(3-Aminopropyl) Triethoxysilane (APTES) Functionalized Magnetic Nanosilica Graphene Oxide (MGO) Nanocomposite for the Comparative Adsorption of the Heavy Metal (Pb(II), Cd(II) and Ni(II)) ions from Aqueous Solution

C Donga
  University of South Africa

S Mishra
  Academy of Nanotechnology and Wastewater Innovations, Johannesburg

A Aziz
  550 University Avenue

L Ndlovu
  University of South Africa

A Kuvarega
  University of South Africa

Ajay Kumar Mishra (✉ ajaykmishraedu@gmail.com)
  KIIT Deemed University   https://orcid.org/0000-0002-3743-8669

Research Article

(3-Aminopropyl) triethoxysilane (APTES) functionalized magnetic nanosilica graphene oxide (MGO) nanocomposite for the comparative adsorption of the heavy metal (Pb(II), Cd(II) and Ni(II)) ions from aqueous solution.

Cabangani Donga[a], Shivani B. Mishra[b], Alaa S. Abd-El-Aziz[c], Llyod N. Ndlovu[a], Alex T Kuvarega[a], Ajay K. Mishra[b,d,e,*]

[a]Institute for Nanotechnology and Water Sustainability, College of Science, Engineering and Technology, University of South Africa, Florida Campus, Johannesburg, South Africa

[b]Academy of Nanotechnology and Wastewater Innovations, Johannesburg, South Africa

[c]University of Prince Edward Island, 550 University Avenue, Charlottetown, Prince Edward Island, Canada

[d]Department of Chemistry, School of Applied Sciences, KIIT Deemed University, India

[e]Research School of Polymeric Materials, Jiangsu, University, China

[*]Corresponding author: ajaykmisharedu@gmail.com

ABSTRACT

(3-aminopropyl) triethoxysilane (APTES) modified magnetic graphene oxide was synthesized and applied in the adsorption of three heavy metals, Pb(II), Cd(II) and Ni(II) from aqueous solution. An approach to prepare magnetic GO was adopted by using (3-aminopropyl) triethoxysilane (APTES) as a functionalizing agent on magnetic nanosilica coupled with GO to form the $Fe_3O_4@SiO_2-NH_2$/GO nanocomposite. FT-IR, XRD, BET, UV, VSM, SAXS, SEM and TEM were used to characterize the synthesized nanoadsorbents. Batch adsorption studies were conducted to investigate the effect of solution pH, initial metal ion concentration, adsorbent dosage and contact time. The maximum equilibrium time was found to be 30 min for Pb(II), Cd(II) and 60 min for Ni(II). The kinetics studies showed that the adsorption of Pb(II), Cd(II) and Ni(II) onto $Fe_3O_4@SiO_2-NH_2$/GO followed the pseudo-second-order kinetics. All the adsorption equilibrium data were well fitted to Langmuir isotherm model and maximum monolayer adsorption capacity for Pb(II), Cd(II) and Ni(II) were 13.46, 18.58 and 13.52 mgg^{-1}, respectively. The $Fe_3O_4@SiO_2-NH_2$/GO adsorbents were reused for at least 7 cycles without the leaching of mineral core, showing the enhanced stability and potential application of $Fe_3O_4@SiO_2-NH_2$/GO adsorbents in water/wastewater treatment.

1.INTRODUCTION

The widespread contamination of clean water resources by toxic, non-biodegradable heavy metal ions occurs from manifold anthropogenic activities [1,2]. The most common heavy metals found in contaminated surface, ground and industrial wastewater include, lead, mercury, chromium, arsenic, cadmium, zinc, copper and nickel [3–5]. Most of these heavy metals are carcinogenic and negatively impact human health even when present in very small concentrations [6,7]. According to the World Health Organization (WHO) standards, the maximum permissible limits in drinking water for Pb(II), Cd(II) and Ni(II) are 0.01 mg/L, 0.03 mg/L and 0.07 mg/L respectively [8–10]. A variety of wastewater treatment methodologies, including precipitation, reverse osmosis, ion exchange and adsorption have been investigated as potential remediation techniques. The adsorption process tops the list of these techniques largely because of simplicity of design, low-cost adsorbents and regenerability of the adsorbents. The growing need for the development of effective, environmentally- friendly and cost effective nano-sized adsorbent materials for the adsorption of heavy metal ions during wastewater treatment has drawn much attention in the scientific research fields[11]. Therefore, the synthesis and application of nanocomposites consisting of graphene oxide (GO) and magnetic nanoparticles gained great attention in the previous decade [12]. The hydrophilic GO exhibits unique physicochemical properties and high surface area due to oxygen moieties on its basal planes and edges. GO has been explored and functionalized for use as an adsorbent in water/wastewater treatment purposes. Studies have shown the presence of a variety of functional groups such as epoxy (C-O-C), hydroxyl (-OH), carboxyl (-COOH) and carbonyl (C=O) on the surface of GO which affords further modification and eventually promotes covalent bonding of desired organic groups on GO surface [8,13–15]. Although GO has good adsorption properties, it still faces post-treatment recovery and long separation time challenges because of its great dispersion in aqueous solution which results in the formation of stable colloidal suspensions. Furthermore, the layers in GO aggregate due to strong inter-planar interactions leading to reduced metal ion adsorption capacity. Magnetic graphene oxide nanocomposites possess a combination of magnetic properties and high surface area. Therefore, the inclusion of low toxicity, highly

magnetic and biocompatible magnetic nanoparticles introduces the advantage of easy separation, wherein the magnetic nanoadsorbent can be separated easily in the presence of an external magnetic field [16–18]. In a previous study, Fe_3O_4 was incorporated with GO/polyethylenimine (PEI), to obtain $RGO/PEI/Fe_3O_4$. The nanocomposite showed a high removal ability on Cr(VI) through adsorption and reduction and excellent magnetic collectability from aqueous solution [19]. A novel functional and magnetic hybrid nanocomposite comprising of graphene oxide (GO)-wrapped magnetite (Fe_3O_4) nanoclusters (Fe_3O_4@GO) by electrostatically driven co-assembly was reported. The nanocomposite was shown to exhibit maximum adsorption capacities of 131.10, 34.50 and 39.95 mg/g for methylene blue (MB), rhodamine B (RhB) and methyl orange (MO), respectively [20]. An efficient 2-mercapto-5-phenylamino-1,3,4-thiadiazole (2-MPATD) modified magnetic graphene oxide was also reported and the nanocomposite were successfully used for the preconcentrative determination of inorganic mercury, Hg(II) ions in water and seafood samples [21]. Accordingly, the aim of this study was to comparatively evaluate the adsorption and quantification of Pb(II), Cd(II) and Ni(II) ions in aqueous solution by applying (3-Aminopropyl) triethoxysilane (APTES) functionalized magnetic graphene oxide (MGO). APTES possess nitrogen-containing functional groups that have a strong coordination ability with heavy metal ions. Hence, modification of MGO with APTES enhances stability and improves other properties such as selective adsorption of metal ions from aqueous solution [22]. To the best of our knowledge, there are no previous literature studies on the comparative adsorption of the heavy metals Pb(II), Cd(II) and Ni(II) using APTES functionalized magnetic graphene oxide (MGO) nanocomposites. The investigated adsorption and desorption behaviour of synthesized nanocomposite material showed that the adsorbent materials were influenced by changes in pH and metal ion concentration. The metal ion adsorption on the Fe_3O_4@SiO_2-NH_2/GO adsorbent followed the order Pb(II) > Cd(II) > Ni(II) due to the presence of functional groups that have a high affinity for Pb(II) and Cd(II) compared to Ni(II) ions.

2.EXPERIMENTAL

2.1. Materials and chemicals

Graphite powder, ammonia solution, conc. H_2SO_4 (98%), H_2O_2 (30%), $KMnO_4$ powder, $NaNO_3$, ferric chloride hydrate ($FeCl_3 \cdot 6H_2O$), ferrous chloride tetrahydrate ($FeCl_2 \cdot 4H_2O$), (3-Aminopropyl) triethoxysilane (APTES), tetraethyl orthosilicate (TEOS), Ethanol and NH_4OH

(25wt%) were purchased from Sigma Aldrich, South Africa. Metal ion salts, $Pb(NO_3)_2$, $Cd(NO_3)_2$ and $NiSO_4.6H_2O$ were purchased from Sigma Aldrich, S.A. All other chemicals in analytical purity were used as supplied without further purification. Distilled water was used for the preparation of the metal ion stock solutions.

2.2. Synthesis of Fe_3O_4 MNPs

Fe_3O_4 nanoparticles were prepared from the iron salts following the chemical coprecipitation method with minor changes [23]. Accordingly, $FeCl_3 \cdot 6H_2O$ (12.54 g) and $FeCl_2 \cdot 4H_2O$ (5.86 g) were dissolved in 300 mL deionized water in 500 mL three-necked flask under an inert N_2 atmosphere at $40^{\circ}C$ using a magnetic stirrer. Thereafter, 50 mL ammonium hydroxide, NH_4OH (25wt%) was added gradually into the iron mixture solution under vigorous stirring at an elevated temperature of $60^{\circ}C$. The reaction temperature was raised to $80^{\circ}C$ and the mixture stirred at pH 10.0 for 2 hours. After 2 hours, the precipitated dark brownish Fe_3O_4 nanoparticles were magnetically separated using an external magnet and washed six times with deionized water and ethanol, then dried in a vacuum oven for 12 hours.

2.3 Synthesis of GO

The synthesis of GO was conducted following the Modified Hummers' method with minor modifications [24,25]. Graphite powder (3.2 g) and $NaNO_3$ (3.2 g) were added into 98% H_2SO_4 (140 mL) in an Erlenmeyer flask (800 mL), in an ice-bath ($< 10^{\circ}C$) with constant stirring. After stirring the mixture for 4 hrs at this temperature, $KMnO_4$ (18.5 g) was gradually added to the suspension under stirring for 1 h below $15^{\circ}C$. To the crude mixture, 300 mL distilled water was gradually added, and the mixture stirred for 2 hrs. The temperature was raised to $35^{\circ}C$ under constant stirring for 2 hrs. Subsequently, 60 mL of a H_2O_2(30%) aqueous solution was added, and the mixture changed colour from dark brown to yellow. The resulting mixture was centrifuged at 4400 rpm for 20 min and then washed repeatedly with 5% HCl solution and then deionized water several times until a neutral pH value of the gel-like substance. After centrifugation the gel-like substance was vacuum dried at $70^{\circ}C$ to give GO powder.

2.4 Synthesis of $Fe_3O_4@SiO_2$-NH_2

The synthesis of $Fe_3O_4@SiO_2$-NH_2 was done through a reflux method [26] with slight modifications. 2.5 g of the $Fe_3O_4@SiO_2$ was dispersed in 100 mL of anhydrous toluene in an ultrasonicator for 30 minutes. To the dispersed $Fe_3O_4@SiO_2$, 1.5 mL APTES was gradually

added. The mixture was refluxed for 6 h at 80˚C under an inert nitrogen atmosphere. The final product was washed three times with ethanol and distilled water, dried in a vacuum oven at 70˚C to obtain $Fe_3O_4@SiO_2-NH_2$.

2.5 Synthesis of $Fe_3O_4@SiO_2-NH_2/GO$ nanocomposites

The cross coupling of $Fe_3O_4@SiO_2-NH_2$ and GO through a covalent bond formation (amide bond) was conducted by modifying a previous method [27]. 1.5 g GO was dispersed in 350 mL of deionized water in a 500 mL conical flask and ultrasonicated for 1 h. To the GO/water dispersion, 0.5 g of N – (3 – dimethylamino propyl)-N-ethyl carbodiimide hydrochloride (EDC) and 0.3 g N- hydrosuccinimide (NHS) were added and the mixture vigorously stirred for 2 h. To the mixture, 3.5 g of $Fe_3O_4@SiO_2-NH_2$ dispersed in water/toluene (2:1) was gradually added under rigorous stirring. The reaction mixture was stirred and further refluxed at 110˚C in a preheated oil bath for 1 h and heated in a Teflon-lined autoclave for 2 h at 150˚C, cooled and magnetically separated. The final product ($Fe_3O_4@SiO_2-NH_2/GO$) was washed with water several times and dried for 48 h at 60˚C.

2.6 Equilibrium Experiments.

In this study, equilibrium adsorption of Pb(II), Cd(II) and Ni(II) on $Fe_3O_4@SiO_2-NH_2/GO$ was conducted out in polyethylene tubes. Various metal ion concentrations and pH values with a constant temperature of 25˚C, using an orbital shaker operating at an agitation speed of 150 rpm were applied. 1000 mg/L stock solutions of metal salts $Pb(NO_3)_2$ for Pb(II), $Cd(NO_3)_2$ for Cd(II) and $NiSO_4$ for Ni(II) were used respectively. Different concentrations of the two metal ions were established by serial dilution of the stock solution. The initial pH of the metal ion solutions was adjusted to the desired range by making use of 0.1 M HCl and 0.1 M NaOH solutions. After magnetic separation and filtration, the solution was analysed for metal ion concentration and ion adsorbed on the adsorbent at equilibrium time using inductively coupled plasma optical emission spectrometry (Nexion 350D ICP-MS/HDC system, Perkin Elmer). The amount of metal ion adsorbed on the adsorbent at equilibrium time, q_e, was calculated following the equation:

$$q_e = V(C_o - C_e)/m \qquad\qquad (1)$$

where C_o is the initial concentrations (mg/L) of the metal ion, C_e is the concentrations (mg/L) of metal ion in solution after the adsorption, V is the volume of solution (L), and m is the mass (g) of $Fe_3O_4@SiO_2-NH_2/GO$.

The percentage ion removal was calculated using equation 2;

Removal rate (%R) = 100 x (C$_o$ – C$_t$)/C$_o$ (2)

 where C_o is the initial concentration of dye solution (mg/L) and C_t is the final concentration (mg/L) after the adsorption process

The adsorption capacity was calculated from the mass of the adsorbent and the volume of the metal ion solution using equation 3;

Adsorption capacity, q$_t$ (mg) =V x (C$_o$ – C$_t$)/m   (3)

 where m is the dose of adsorbent (mg) and V is the volume of the metal ion solution (L).

2.7 Regeneration and reusability studies

Desorption experiments were conducted by mixing 30 mg of the Fe$_3$O$_4$@SiO$_2$-NH$_2$/GO material containing adsorbed metal ions, Pb(II), Cd(II) and Ni(II) with 30 mL 0.1 M HNO$_3$. The mixture was shaken for 3 h at 180 rpm at room temperature and magnetically separated through the application of an external magnetic field. The adsorbent material was rinsed with de-ionized water and dried overnight at 60˚C and reused for the adsorption studies. This procedure was repeated 7 consecutive times. The concentration of metal ions in the filtrate was determined by using the inductively coupled plasma mass spectrometry (ICP-MS) (Perkin Elmer).

2.8 Adsorbent Characterization

The crystalline structure and phase purity of the nanoparticles were identified using the X-ray diffraction (XRD) patterns recorded using Rigaku Smart Lab X-Ray Diffractometer at room temperature using Cu-Kα radiation (λ=0.154059 nm) operated at 45 kV and 200 mA in the 2θ range of 5–80° and a scan speed of 2°/min. Small-angle x-ray scattering (SAXS) spectroscopy was performed with SAXS Spectrometer from Anton-Paar, South Africa. The X-ray scattering spectra were plotted with a SAX drive software. GIFT software was used to Fourier transform the scattering data to obtain the pair distance distribution function (PDDF) and size distribution spectra. A Lambda 650S UV-Vis spectrophotometer (Perkin - Elmer) was used for UV-Vis measurements. Magnetic properties were measured using the Vibrating Sample Magnetometry at room temperature (VSM). The surface morphologies of the synthesized materials were obtained on a JOEL JSM-7800F Field Emission Scanning Electron Microscope (FESEM) coupled with Thermo Scientific Ultra dry EDS detector. High-resolution transmission electron microscopy (HRTEM) images of powders were taken

using a Tecnai TF20 at an acceleration voltage of 200 kV. The zeta potential was measured at various pH with Malvern Nanosizer ZS (Malvern, UK).

3.0 RESULTS AND DISCUSSION

3.1 FTIR analysis

$Fe_3O_4@SiO_2-NH_2/GO$ nanocomposite were synthesized through an immediate bioconjugation that involved the formation of amide bonds between amine groups of APTES and the carboxyl functionality of GO. The functionalities in the nanomaterials were confirmed through FTIR measurements shown in Fig. 1.
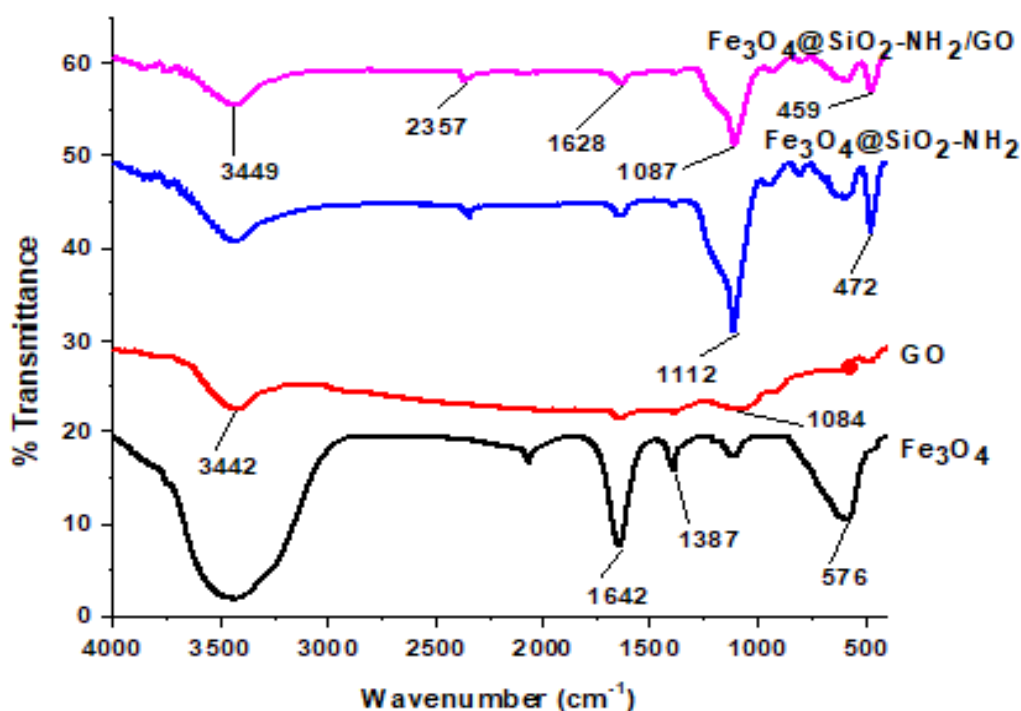

Fig. 1. The FTIR spectra of Fe_3O_4, GO, $Fe_3O_4@SiO_2-NH_2$ and $Fe_3O_4@SiO_2-NH_2/GO$.

Fe_3O_4 clearly reveals the presence of a strong band at 576 cm^{-1} corresponding to the stretching vibration of the Fe-O [28]. The other two bands observed at 1642 and 3449 cm^{-1} arises due to Fe-OH bending and O-H stretching vibrations from the adsorbed water molecules on the silica shell. The coating of Fe_3O_4 nanoparticles with silica and further modification with an amine group showed peaks at 1087 cm^{-1} and 459 cm^{-1} which were a

result of asymmetric stretching vibrations of the Si-O-Si bond, the symmetric stretching of Si-O-Si, and the bending vibration of the Si- OH bond, respectively [29]. The C-H stretching vibration of the hydrocarbon chains from APTES was depicted by the peak at 2357 cm^{-1}. The reaction of amino group from $Fe_3O_4@SiO_2-NH_2$ and the carboxyl functionality from the GO nanosheets through an amide bond formation resulted in the formation of $Fe_3O_4@SiO_2-NH_2$/GO (Fig. 1). The new and characteristic band at 1628 cm^{-1} corresponds to the amide carbonyl group (-CONH) which confirms the successful covalent bonding of the $Fe_3O_4@SiO_2-NH_2$ to the GO nanosheets. The band at 3449 cm^{-1} and 3442 cm^{-1} showed that the synthesized adsorbents have suitable surfaces for hydrogen bonding interactions [30]. Oxygen functional groups in GO confirmed by characteristic bands at 3442 cm^{-1} (O–H stretching vibrations) and at 1084 cm^{-1} (C–O stretching vibrations).

3.2 UV-Vis spectra for the nanocomposites

The UV-Vis spectra for GO and $Fe_3O_4@SiO_2-NH_2$/GO (Fig. 2) shows the maximum absorbance peaks at λmax 248 nm and 253 nm, respectively. These two spectra confirmed the successful synthesis of GO and its presence in the $Fe_3O_4@SiO_2-NH_2$/GO nanocomposite. The characteristic peak of GO observed at 248 nm, originate from the π→π* transitions that occur in aromatic C–C and C=C bonds found in sp^2 hybrid centres of GO [31,32]. $Fe_3O_4@SiO_2-NH_2$/GO spectrum showed typical results due the presence of dominant and characteristic groups of GO in the nanocomposite, therefore the major peak observed at 253 nm can be attributed to the n-π* transitions of the C=O bonds in sp^3 hybrid domains.
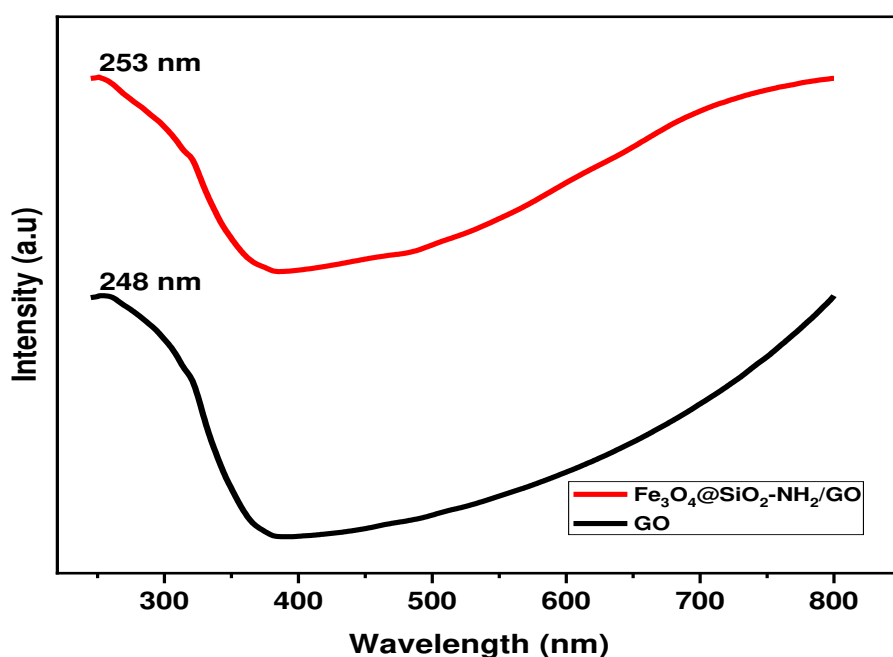
Fig. 2. UV spectra of the nanocomposites GO and $Fe_3O_4@SiO_2$-NH_2/GO.

3.3 VSM measurements

The magnetic properties of Fe_3O_4 and $Fe_3O_4@SiO_2$-NH_2/GO were measured by VSM at room temperature (Fig. 3). The hysteresis loops showed ferromagnetic behaviour of the synthesized nanocomposites. Magnetic saturation values are 68.5 and 29 emu/g for Fe_3O_4 and $Fe_3O_4@SiO_2$-NH_2/GO, respectively. Data analysis of the saturation magnetization values revealed a decrease from 68.5 to 29 emu/g. This trend indicated the influence of silica coating on the surface of Fe_3O_4 and subsequent amino functionalization ($Fe_3O_4@SiO_2$-NH_2/GO) on the magnitude of magnetic saturation.
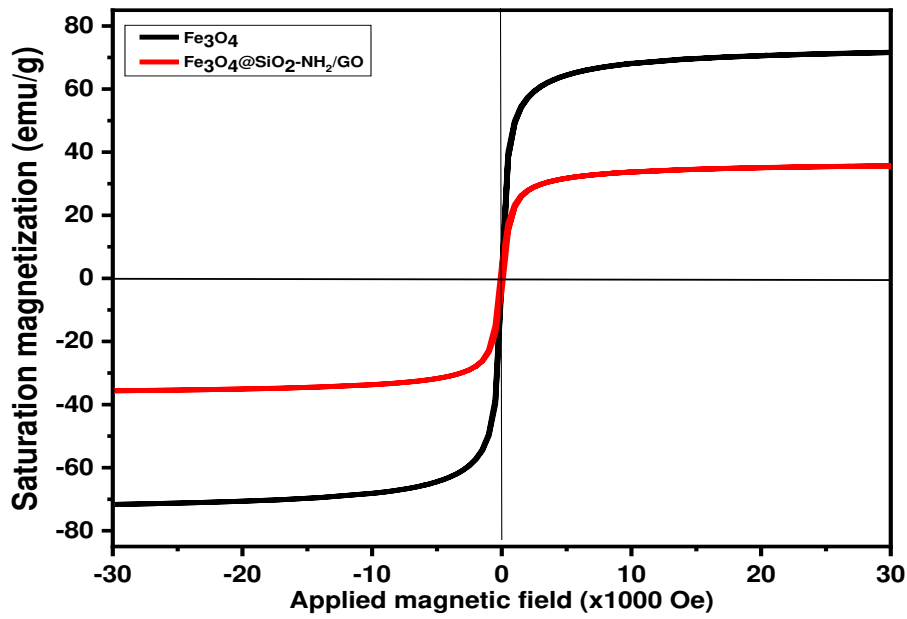
Fig. 3. Magnetic hysteresis loops of Fe_3O_4 and $Fe_3O_4@SiO_2$-NH_2/GO measured at room temperature.

The degree of saturation magnetization showed the favourable extent of magnetic separation of the $Fe_3O_4@SiO_2$-NH_2/GO adsorbent from aqueous solution when an external magnetic field is applied.

3.4 XRD analysis

The XRD results (Fig. 4), show that the phase structure of GO in $Fe_3O_4@SiO_2$-NH_2/GO nanocomposites becomes amorphous from the hybridization. Furthermore, the dominant diffraction peaks at $2\theta = 35.6°$, $43.3°$, $57.0°$ and $62.6°$ in $Fe_3O_4@SiO_2$-NH_2/GO can be assigned to (311), (422), (511) and (440) crystal planes of Fe_3O_4, respectively. These characteristic peaks are in agreement with the JCPDS card (19-0629) [33]. Also, the intense peak (311) shows the order and growth of crystalline planes follows a similar diffraction pattern to that of Fe_3O_4 core with no significant changes, except for the decrease in peak intensity of Fe_3O_4 from the formation of amorphous structure of silica coating on the Fe_3O_4 nanoparticles. The structural arrangement, oxidation degree and phase purity of the nanocomposites were observed from the XRD data. The average particle size (L) of Fe_3O_4 nanomaterial estimated from breadths of reflection of the (311) peak at $2\theta = 35.6°$ according to the Scherrer equation was 13.5 nm.

$$L = \underline{\frac{K\lambda}{}} \qquad\qquad (4)$$

$$\beta Cos\ \theta$$

where K is the shape factor usually assigned as 0.9, λ is the wavelength used (1.54 06), and β is the full width at half-maximum (in rad) of the diffraction peak. The respective peak intensities of spectra in (Fig. 4) do not exhibit widespread topological structural variation from the composition of pure Fe_3O_4 upon coating and functionalization showing that the magnetic nanoparticle phase in most samples (with exception of GO) has the dominant mass contribution. Literature studies confirmed that the XRD diffraction peak at $2\theta = 11.6°$ can be assigned to (002) [34].
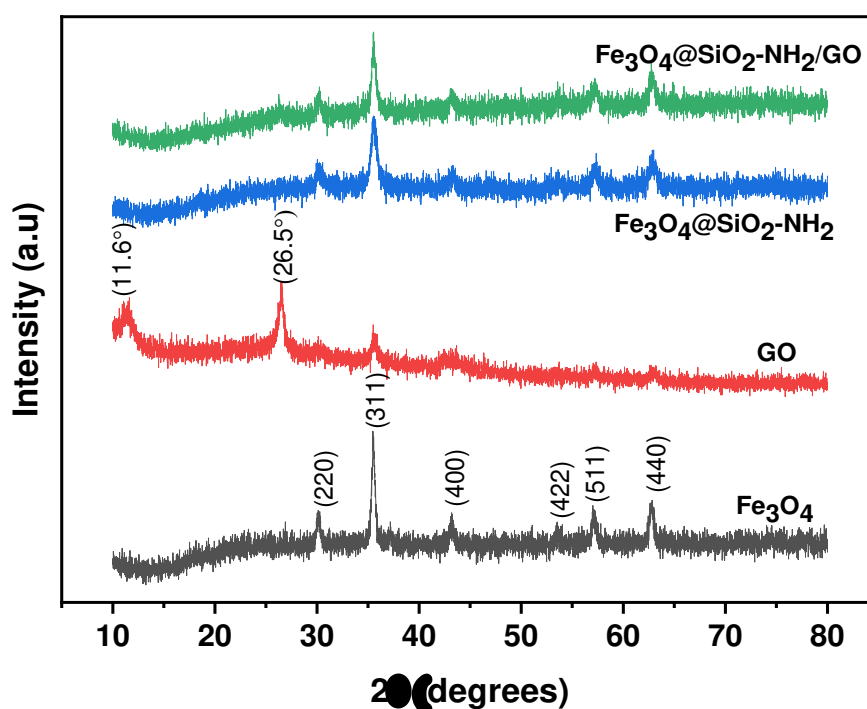

Fig. 4. XRD spectra of Fe_3O_4, GO, $Fe_3O_4@SiO_2-NH_2$ and $Fe_3O_4@SiO_2-NH_2/GO$.

3.5 SEM analysis

The surface morphologies of the synthesized materials were examined by field emission scanning electron microscopy (FE-SEM, JEOLJSM-7000F) as shown in Fig. 5(a)-(e). FE-SEM results for Fe_3O_4, (Fig. 5(a)) show the aggregated and semi-spherical Fe_3O_4 particles because of strong magnetic dipole-dipole attractions between particles [35]. Slight changes were observed in the surface morphology for the silica coated $Fe_3O_4@SiO_2$ (Fig. 5(b)) and amino functionalized magnetic nanosilica ($Fe_3O_4@SiO_2-NH_2$) nanocomposites. After functionalization, there was an observed increase in the surface roughness (Fig. 5(c)). The

GO image (Fig. 5(d)) shows a sheet-like structure of synthesized GO, with rough and regular external surfaces decorated with wrinkles. These wrinkles are loaded with reactive oxygen functional groups [36]. $Fe_3O_4@SiO_2-NH_2/GO$ adsorbent material (Fig. 5(e)) shows a rough external surface due to the attachment of amino functionalized magnetic nanosilica ($Fe_3O_4@SiO_2-NH_2$) on the surface of GO sheets through amide bond formation (-CONH). The presence of amide bonds ensures the stability of the $Fe_3O_4@SiO_2-NH_2/GO$ nanocomposite material.
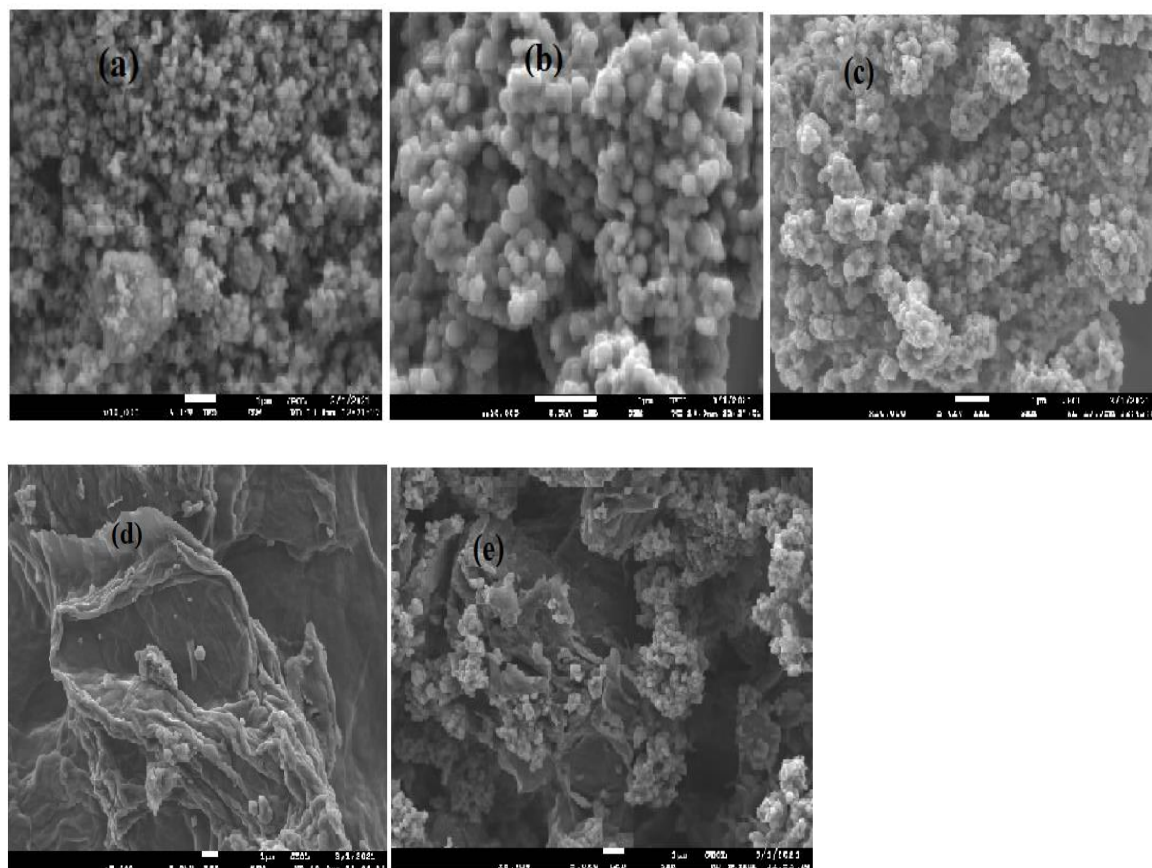

Fig. 5. SEM of a) Fe_3O_4, b) $Fe_3O_4@SiO_2$, c) $Fe_3O_4@SiO_2-NH_2$ d) GO and e) $Fe_3O_4@SiO_2-NH_2/GO$.

3.6 TEM analysis

The internal morphology of the nanocomposites Fe_3O_4, $Fe_3O_4@SiO_2-NH_2$, and $Fe_3O_4@SiO_2-NH_2/GO$ (Fig. 6(a)-(c)) were studied using HRTEM and showed the spherical shape of the magnetic nanoparticles with an average particles size ranging from 12–18 nm [37]. The Fe_3O_4 nanoparticles (Fig. 6(a) showed enhanced particle aggregation compared to the silica coated and amino functionalized magnetic nanosilica, $Fe_3O_4@SiO_2-NH_2$ (Fig. 6(b). ImageJ software was used to calculate the average particle size by measuring the diameters of 100

nanoparticles each of Fe_3O_4 and $Fe_3O_4@SiO_2$-NH_2 nanoparticles, respectively. The amino functionalized magnetic nanosilica were successfully deposited on the surfaces of GO sheets through amide bond (-CONH) formation as shown in Fig. 6(e). $Fe_3O_4@SiO_2$-NH_2 nanoparticles are attached onto the GO sheets, where characteristic wrinkles are present. The wrinkles are widely dispersed in areas with abundant oxygen groups (Fig. 6(c)). The distribution curves (Fig 6(d) – (e) showed the average particle size of 13.5 nm for Fe_3O_4 nanoparticles and 17 nm for amine functionalized magnetic nanosilica, $Fe_3O_4@SiO_2$-NH_2, confirming the presence of additional material embedded on the magnetite core.

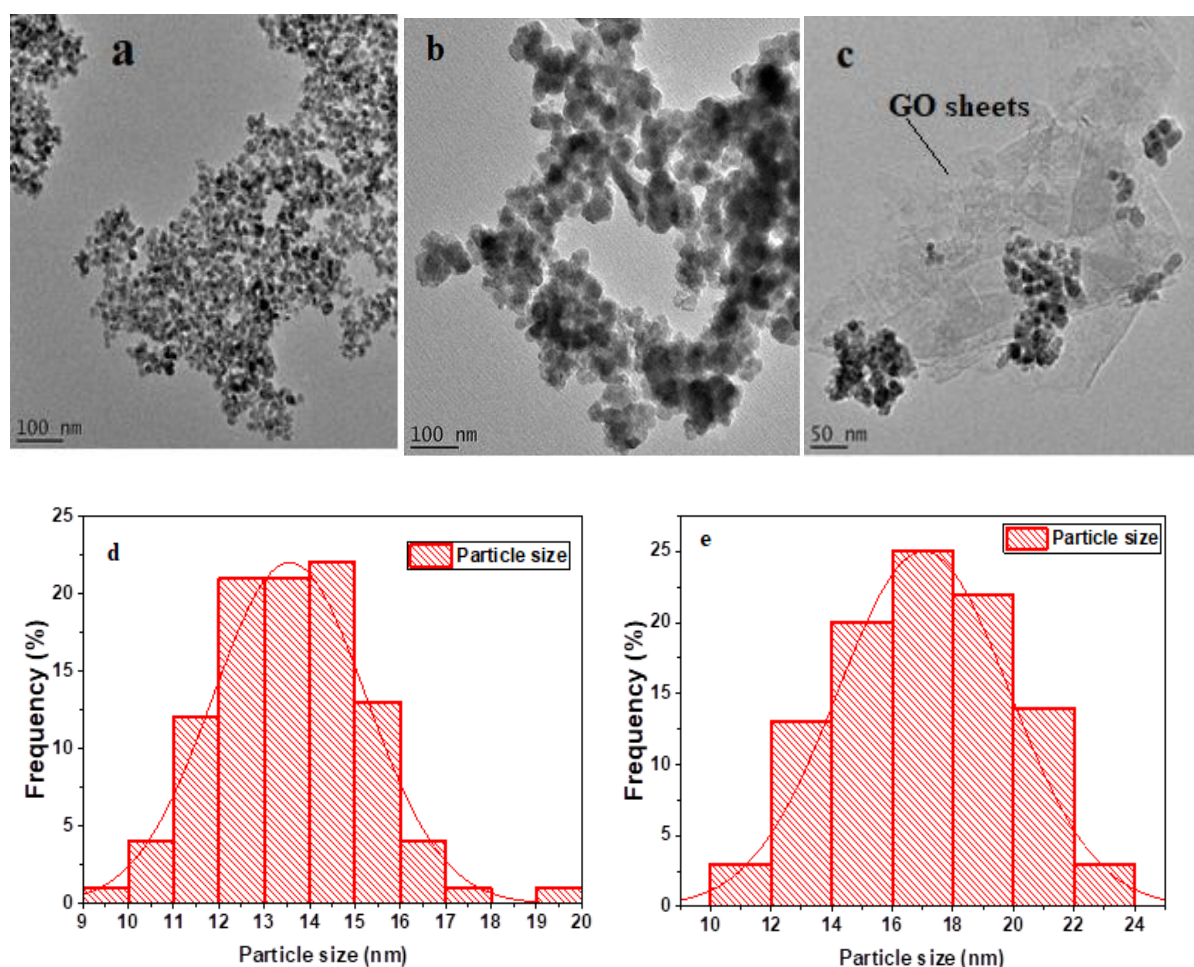Fig. 6. TEM of a) Fe_3O_4, b) $Fe_3O_4@SiO_2$-NH_2 and c) $Fe_3O_4@SiO_2$-NH_2/GO and particle size distributions for d) Fe_3O_4 and e) $Fe_3O_4@SiO_2$–NH_2.

3.7 BET N_2 adsorption–desorption analysis

The N_2 adsorption–desorption isotherms curves of Fe_3O_4 nanoparticles and $Fe_3O_4@SiO_2$–NH_2/GO nanocomposite are shown in Fig. 7. These isotherms were measured at 77 K. The measured BET surface areas of the Fe_3O_4 nanoparticles and $Fe_3O_4@SiO_2$–NH_2/GO adsorbent

material were 19.76 and 34.48 m^2g^{-1}, respectively. Therefore, the microporous $Fe_3O_4@SiO_2-$NH_2$/GO adsorbent showed a specific surface area (34.48 m^2g^{-1}) due to APTES functionalization, total pore volume (5.84 cm^3g^{-1}) and average pore diameter (19.58 nm) compared to less porous Fe_3O_4 (Table 1). Adsorbents with a high surface area and porous structure usually show an increased adsorption capacity for the target adsorbates.

Table 1. Experimental data on textural properties of Fe_3O_4 and $Fe_3O_4@SiO_2$-NH$_2$/GO.

Magnetic material	Specific surface area BET (m^2g^{-1})	Pore diameter (nm)	Total Pore Volume $(cm^{-3}g)$
Fe_3O_4	19.76	32.24	2.96
$Fe_3O_4@SiO_2$-NH$_2$/GO	34.48	19.58	5.84

The BET specific area, pore diameter and total pore volume indicated the presence of mesoporous $Fe_3O_4@SiO_2-$NH$_2$/GO adsorbent material since its pore diameter is less than 50 nm. This therefore indicates that the adsorption of Pb(II), Cd(II) and Ni(II) from aqueous solution will be greatly enhanced following the increased pore volume and large surface area of $Fe_3O_4@SiO_2-$NH$_2$/GO. The reduction in pore diameter with increase in surface area and pore volume is characteristic with literature studies [38,39].
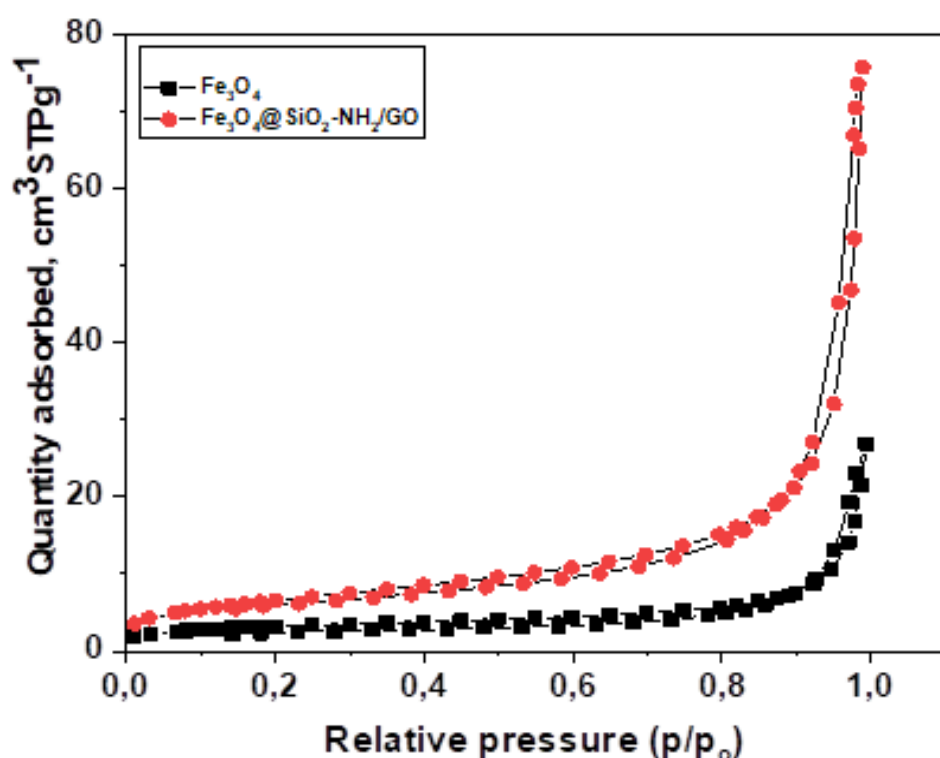
Fig. 7. Nitrogen adsorption–desorption isotherms of Fe_3O_4 and $Fe_3O_4@SiO_2$-NH_2/GO nanocomposite at 77 K.

3.8 SAXS analysis

Small-angle X-ray scattering (SAXS) measurements were used to confirm pore morphology, particle size distribution and architecture within the nanocomposites [40]. The results from the SAXS analyses of $Fe_3O_4@SiO_2$-NH_2/GO were Fourier-transformed, using the GIFT software, into a pair distance distribution function (PDDF) as presented in Fig. 8. The material exhibited a characteristic dumbbell shaped PDDF spectrum at the beginning, with maximum radii of 10.17 nm and 44.64 nm. Unsymmetrical shape of its PDDF indicates a great deal of aggregation of smaller particles.
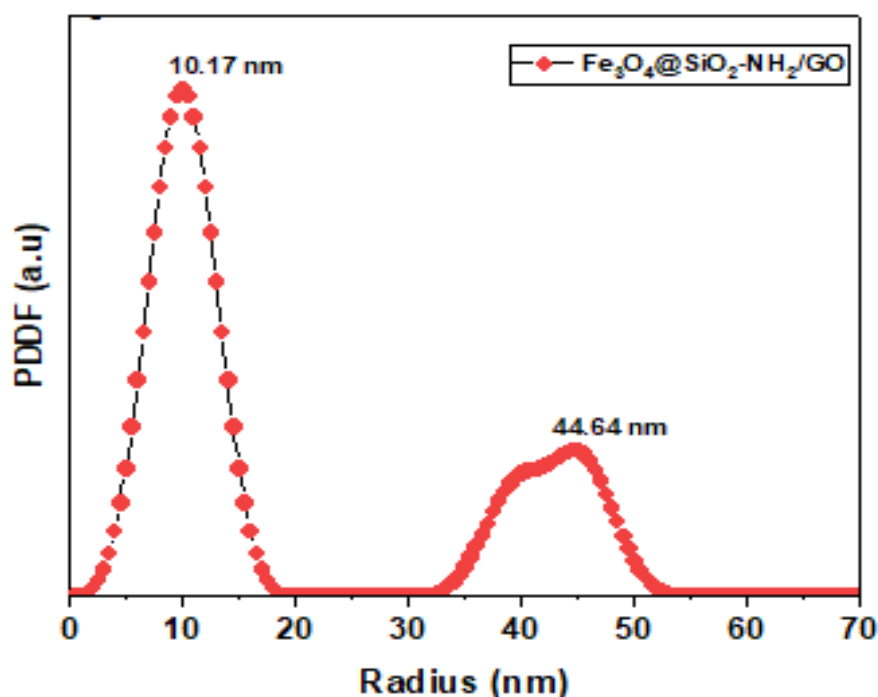

Fig. 8. Small-angle X-ray scattering (SAXS) spectrum showing of Pair-distance distribution function (PDDF) for $Fe_3O_4@SiO_2$-NH_2/GO.

3.9. ADSORPTION EXPERIMENTS

3.9.1 Zeta potential measurements

The zeta potential measurements were conducted on the $Fe_3O_4@SiO_2$-NH_2/GO adsorbent within a pH range of 3 – 11 (Fig. 9). Very low pH conditions increased protonation of

functional groups on GO sheets and amine groups of the adsorbent to give -NH_3^+ active sites [41]. The resulting electropositivity of $Fe_3O_4@SiO_2$-NH_2/GO reduced the rate of adsorption and subsequently the Pb(II), Cd(II) and Ni(II) removal efficiency. The isoelectric point was found for~ pH 4.8, therefore, $Fe_3O_4@SiO_2$-NH_2/GO possesses a negative charge $\leq$ 4.8 and possess a positive charge $\geq$ 4.8.
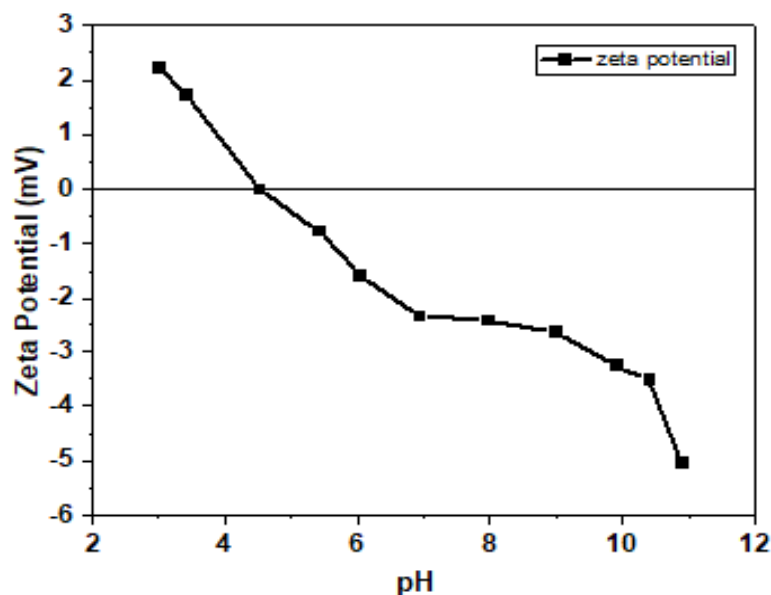
Fig. 9. Zeta potential measurements for $Fe_3O_4@SiO_2$-NH_2/GO.

3.9.2.1 Effect of solution pH

The pH is a key factor to be evaluated in the adsorption process that occurs between adsorbent and adsorbate particles. Furthermore, the surface binding sites on the adsorbent will be exposed more effectively for adsorbing the adsorbate depending on the acidic or alkaline nature of the media [42]. pH affects the adsorption process by influencing the level of protonation of the functional groups on the adsorbent surface and alters the surface charge of the adsorbent [43]. The metal removal efficiency increased with increasing pH until weak acidic to neutral pH range (Fig. 10(a)). The optimum pH for the removal of the metal ions were pH 6 for Ni(II) and 7 - 7.5 for both Cd(II) and Pb(II). The maximum percentage removal efficiencies were 69.92% for Pb(II), 66.57% for Cd(II) and 56.59% for Ni(II), respectively. The pH of natural water is usually in the neutral range [44]. From the pH studies, the $Fe_3O_4@SiO_2@NH_2$/GO adsorbent showed metal ion adsorption affinity in the trend Pb(II) > Cd(II) > Ni(II). At low pH values (< 7), there will be great competition for the negatively charged active sites on the adsorbent between the positively charged divalent metal ions and the hydrogen ions in solution, therefore, the following species of Pb(II) exist in solution Pb(II), $Pb(OH)^+$, $Pb(OH)_2$, $Pb(OH)_3^-$ and $Pb(OH)_4^{2-}$ [45–47]. At alkaline pH

ranges (> 7), there were other Pb(II) species in solution, among them being Pb(OH)$^+$ and Pb(OH)$_2$. Accordingly, the negatively charged adsorbent surface electrostatically attracted Pb(II) in a selective way [48]. Various species of Cd(II) exist in solution and their proportions differ depending on the solution pH, among them are Cd(II), Cd(OH)$^+$, Cd(OH)$_2$, and Cd(OH)$_3$ with the Cd(II) being the dominant species at acidic pH values. The Ni(II) species in aqueous environment were shown to be dependent on pH changes. At different pH values, the Ni(II) exists as Ni(OH)$^+$, Ni(OH)$_4$$^{2-}$, Ni(OH)$_3$$^-$and Ni(OH)$_2$^{o}, with the Ni(II) and Ni(OH)$^+$as the predominant species at low pH ranges [49].
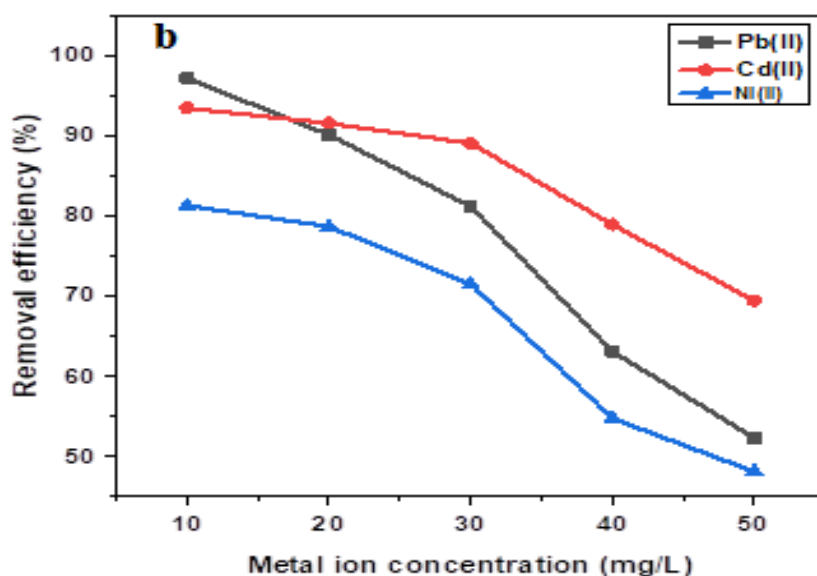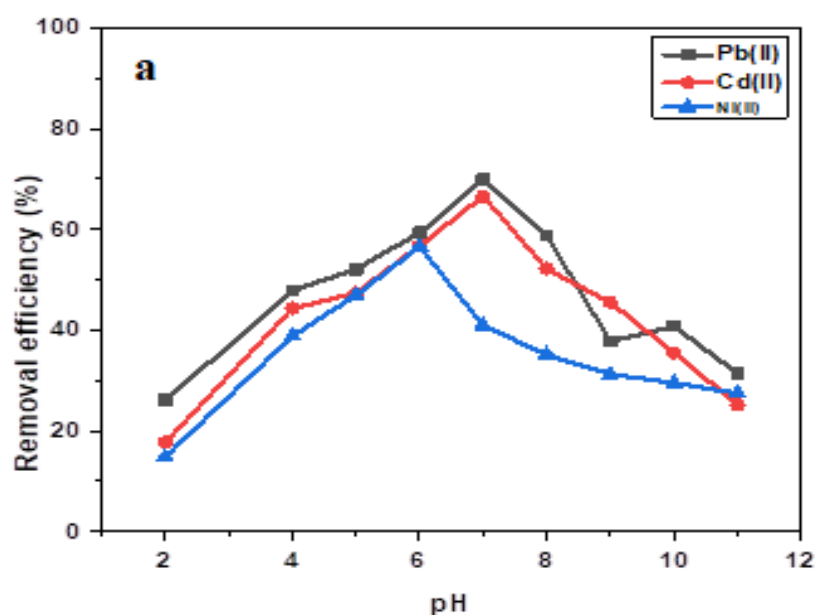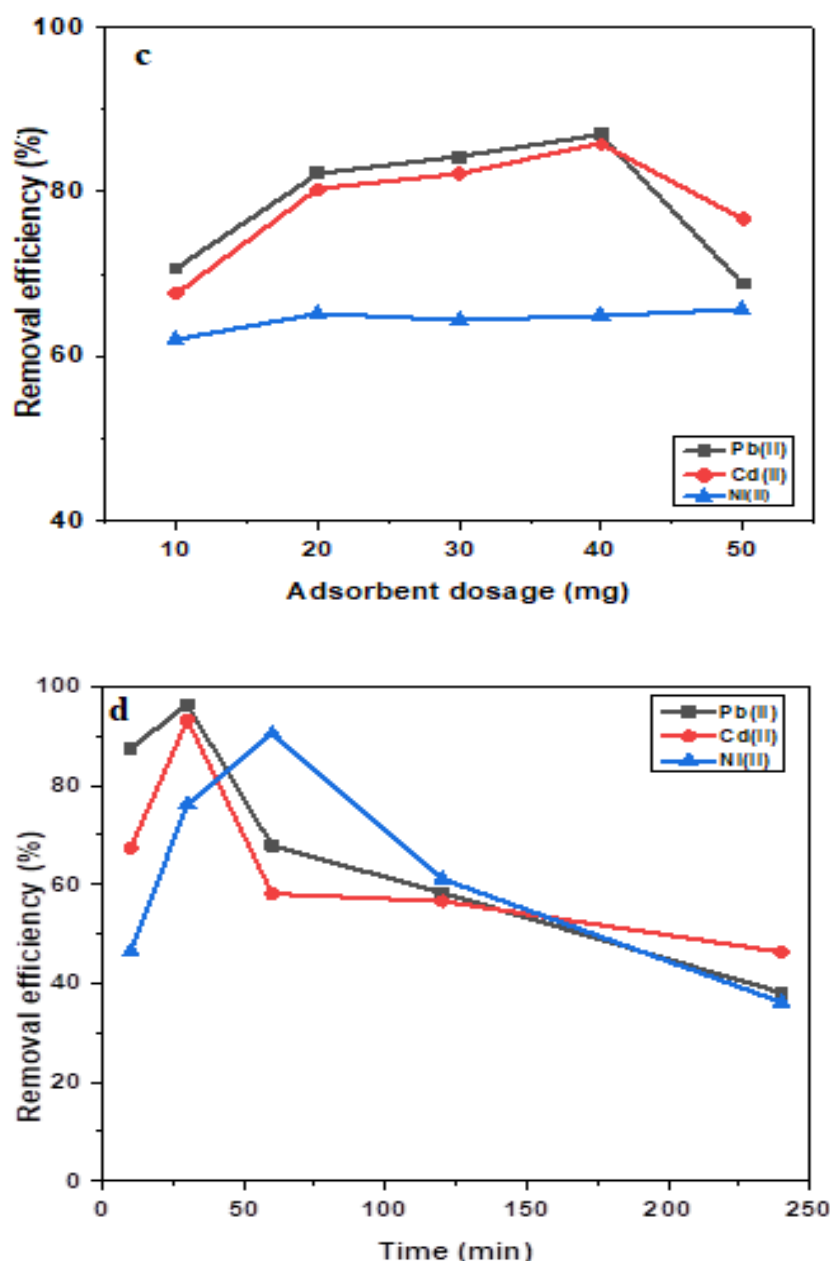
Fig. 10. (a) Effect of pH, (b) effect of metal ion concentration, (c) effect of adsorbent dosage and (d) effect of time on the removal efficiency of the metal ions Pb(II), Cd(II) and Ni(II), using $Fe_3O_4@SiO_2$-NH_2/GO.

3.9.2.2 Effect of initial metal ion concentration

The effect of initial metal ion concentration in the adsorption of Pb(II), Cd(II) and Ni(II), onto $Fe_3O_4@SiO_2$-NH_2/GO was studied from 10 mg/L to 50 mg/L at a pH of 7 - 7.5 for Pb(II) and Cd(II) and pH 6 for Ni(II). The concentration studies showed a favourable initial concentration of 10 mg/L (Fig. 10(b)) for all the three metal ions. From Fig. 10(b), the adsorption increased at a low metal ion concentration due to a good number of binding sites

on the $Fe_3O_4@SiO_2$-NH_2/GO adsorbent, reaching 97.5%, 92.5% and 81.3% for Pb(II), Cd(II) and Ni(II), respectively [50]. Further increase in initial metal ion concentration had no effect on the adsorption due to saturation of binding sites on the adsorbent surface[4].

3.9.2.3 Effect of adsorbent dosage

The influence of adsorbent dosage on the adsorption of the metal ions Pb(II), Cd(II) and Ni(II), ranging from 10 mg to 50 mg at room temperature and constant initial metal ion concentration was investigated (Fig. 10(c)). There was an increase in percentage removal for metal ions with increase in adsorbent dosage due to the availability of more adsorption sites on the adsorbent for metal ion adsorption [47]. This increase in trend reached an equilibrium point at 40 mg of adsorbent dose for Pb(II) and Cd(II), while a constant trend in the adsorption of metal ions with increase in adsorbent dosage was shown for Ni(II). The functional groups on the synthesized $Fe_3O_4@SiO_2$-NH_2/GO adsorbent showed selective adsorption for Pb(II) and Cd(II) ions compared to Ni(II) ions.

3.9.2.4 Effect of contact time

The effect of contact time of adsorption properties of $Fe_3O_4@SiO_2$-NH_2/GO adsorbents was investigated. Fig. 10(d) shows the results of the influence of contact time (10, 30, 60, 120, 240 min) on the removal efficiency of Pb(II), Cd(II) and Ni(II). Maximum removal for Pb(II) and Cd(II) were attained within 30 minutes contact time, while Ni(II) took 60 minutes to reach maximum removal. This was due to the availability of more adsorption sites on the $Fe_3O_4@SiO_2$-NH_2/GO surface at the initial stages. Further increase of contact time did not influence the adsorption of metal ions much because the adsorption sites were already saturated [51]. This was evidenced by the decrease in removal efficiency with increase in contact time from 60 – 240 min. The decrease in removal efficiency with increase in time showed that once the saturation point is reached, further increase in time could no longer influence the adsorptive performance properties of the adsorbent material.

3.9.3 Comparative adsorption

The comparative adsorption data (Fig. 11) for the metal ions Pb(II), Cd(II) and Ni(II), on $Fe_3O_4@SiO_2$, $Fe_3O_4@SiO_2$-NH_2 and $Fe_3O_4@SiO_2$-NH_2/GO showed varied degrees of affinity for Pb(II), Cd(II) and Ni(II) ion adsorption. All the three synthesized adsorbents showed increased metal ion adsorption with increase in the initial pH until circumneutral range. Furthermore, the acidic pH promoted protonation of functional groups on the adsorbent, while the alkaline pH promoted metal ion precipitation, therefore, the circumneutral pH

favoured metal ion removal from aqueous solution [44,52]. The removal efficiency of the metal ions by adsorbents occurred in the order Pb(II) > Cd(II) > Ni(II) confirming enhanced chelation for Pb(II) compared to Cd(II) and Ni(II) ions. The increase in binding sites on the adsorbent surface increased in the order: $Fe_3O_4@SiO_2$ < $Fe_3O_4@SiO_2$-NH_2 < $Fe_3O_4@SiO_2$-NH_2/GO due to presence of more functionalities. Therefore, $Fe_3O_4@SiO_2$-NH_2/GO exhibited better adsorption performance for Pb(II), Cd(II) and Ni(II) ions than $Fe_3O_4@SiO_2$-NH_2 and $Fe_3O_4@SiO_2$. From the results, amino groups from APTES and different functionalities on GO played the major roles in the removal of Pb(II), Cd(II) and Ni(II) ions through chelation.
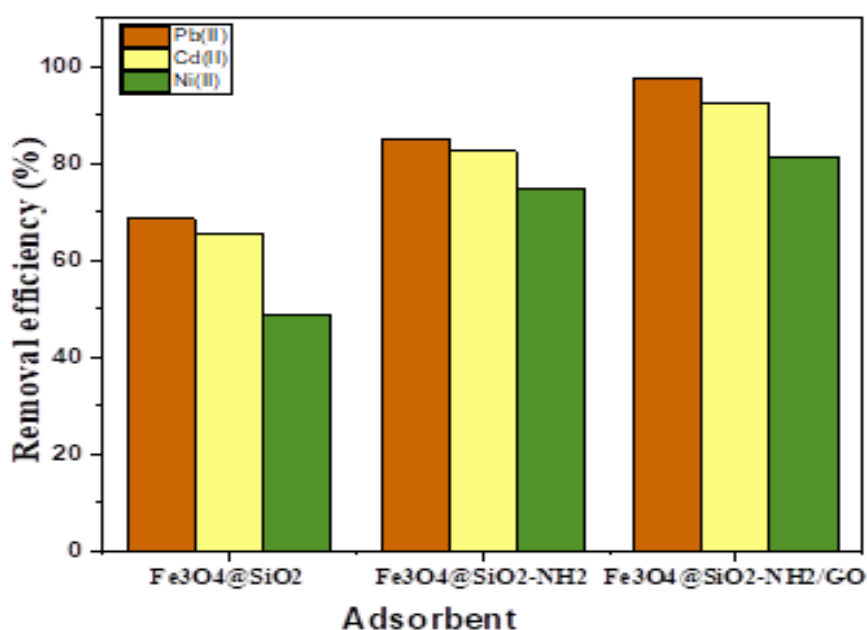

Fig. 11. Comparison of removal efficiency of Pb(II), Cd(II) and Ni(II) by $Fe_3O_4@SiO_2$, $Fe_3O_4@SiO_2$-NH_2 and $Fe_3O_4@SiO_2$-NH_2/GO adsorbents. Initial concentration of 10 mg/L; adsorbent dose: 30 mg; Vol: 30 mL; pH 7-7.5 for Pb(II), Cd(II) and pH 6 for Ni(II) at room temperature.

3.9.4 Regeneration and Stability of Adsorbent

The reusability and stability of an adsorbent are critical factors in the wastewater treatment process. Therefore, the adsorption capacity and level of desorption of the adsorbent under favourable conditions provides information on the potential regeneration and reusability of the adsorbent [26]. The results of this investigation showed the suitability of the $Fe_3O_4@SiO_2$-NH_2/GO adsorbent for the adsorption of both Pb(II) and Cd(II) ions compared to Ni(II) ions.
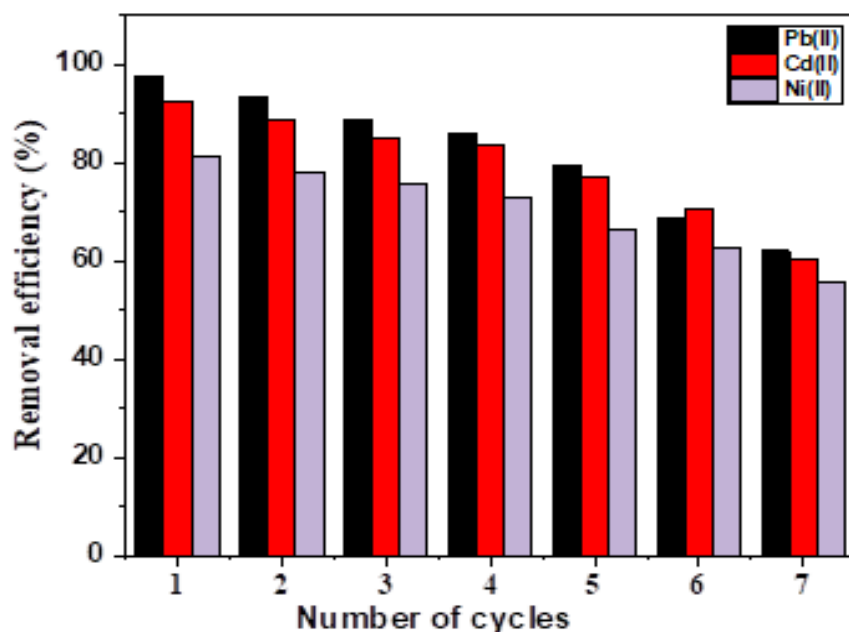
Fig. 12. Removal efficiency of Pb(II), Cd(II) and Ni(II) on Fe_3O_4@SiO_2-NH_2/GO adsorbents after 7 repetitive cycles.

The adsorbent material Fe_3O_4@SiO_2-NH_2/GO showed a steady decrease in removal efficiency from 97.5%, 92.5% and 81.3% for the metal ions Pb(II), Cd(II) and Ni(II), starting from their first absorption– desorption cycle until the seventh cycle (Fig. 12). This decrease was ascribed to the decreasing adsorption sites on the adsorbent surface due to corrosive effect of the 0.1 M HCl used during desorption [53]. A close assessment of the adsorption– desorption cycles showed some reusability, chemical stability, and great application potential for Fe_3O_4@SiO_2-NH_2/GO adsorbent in metal ion removal processes from water/wastewater.

3.9.5 Adsorption isotherms

To investigate the equilibrium concentration of a solute on the surface of an adsorbent to the concentration of the solute in the liquid, at a specific temperature, both Langmuir and Freundlich adsorption isotherms (Fig. 13(a) – (b)) were applied. The Langmuir adsorption isotherm describes the formation of a monolayer adsorbate on the outer surface of the adsorbent material [54]. Langmuir isotherm only holds true for monolayer adsorption onto a surface containing a finite number of identical sites. The model assumes uniform energies of adsorption onto the surface and no transmigration of adsorbate in the plane of the surface. Langmuir isotherm is represented by the following equation:
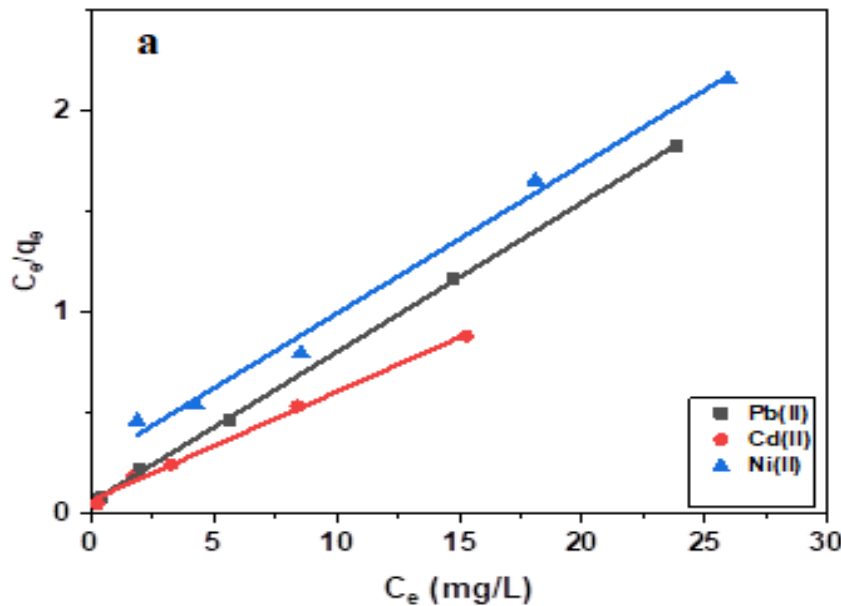
$$1/q_e = 1/Q_o + 1/Q_oK_LCe \qquad (5)$$

where C_e is the equilibrium concentration of adsorbate (mg/L), q_e is the amount of metal adsorbed per gram of the adsorbent at equilibrium (mg/g), Q_o is the maximum monolayer coverage capacity (mg/g) and K_L is the Langmuir isotherm constant (L/mg).

The values of q_e and K_L were calculated from the slope and intercept of the Langmuir plot of C_e versus Ce/q_e (Fig. 13(a)). The Langmuir isotherm $(R)^2$ values were 0.99956, 0.99461 and 0.98876 for Pb(II), Cd(II) and Ni(II), respectively. Furthermore, the equilibrium parameter R_L, which is a dimensionless constant known as the separation factor or equilibrium parameter expresses the essential features of the Langmuir isotherm.

$$R_L = \frac{1}{1 + (1 + K_L Co)}$$

(6)

where C_o is the initial concentration, K_L is the Langmuir constant related to the energy of adsorption. The R_L value indicates the adsorption nature to be either unfavourable if $R_L > 1$, linear if $R_L = 1$, favourable if $0 < R_L < 1$ and irreversible if $R_L = 0$. In this study, the R_L values of Pb(II), Cd(II) and Ni(II) were 0.0727, 0.1003 and 0.2033, respectively. Therefore, the adsorption nature was favourable with Langmuir isotherm for all the three metal ions since their values were within the range $0 < R_L < 1$.
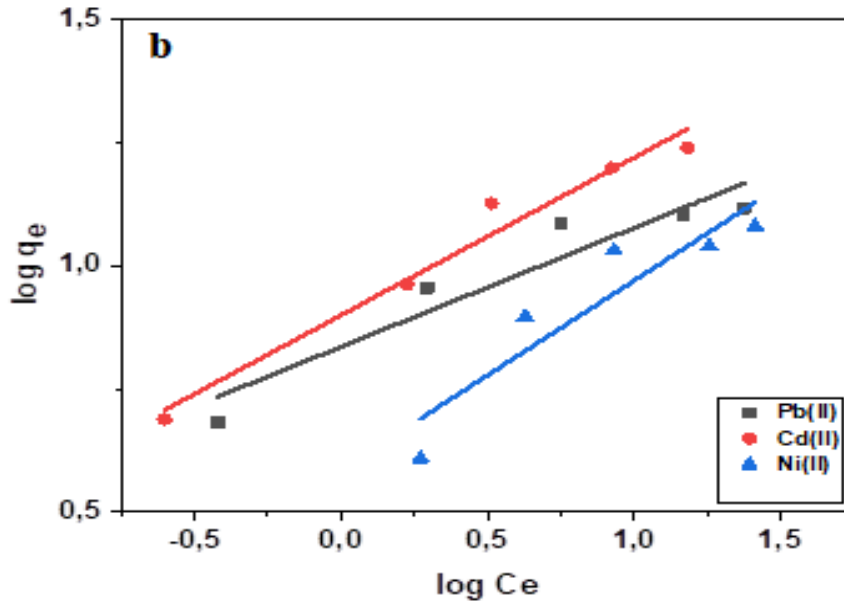
Fig. 13. a) Langmuir isotherm and b) Freundlich isotherm for adsorption of Pb(II), Cd(II) and Ni(II) $Fe_3O_4@SiO_2-NH_2/GO$.

The Freundlich isotherm focuses on the adsorption on a heterogeneous surface of the adsorbent material [55]. The data for the Freundlich isotherm is often represented by the empirical equation:

$$q_e = K_f(C_e)^{1/n} \tag{7}$$

where K_f is the Freundlich isotherm constant (mg/g), n is the adsorption intensity, C_e is the equilibrium concentration of adsorbate (mg/L) and q_e is the amount of metal adsorbed per gram of the adsorbent at equilibrium (mg/g). The Freundlich isotherm for this study ((Fig. 13(b)) coupled with the results from Table 2 showed the unfavorability of this isotherm for the results of this study. The constant K_f is an approximate indicator of adsorption capacity, while 1/n is a function of the strength of adsorption in the adsorption process. K_f and n are parameters characteristic of the sorbent-sorbate system, which must be determined by data fitting and whereas linear regression is generally used to determine the parameters of kinetic and isotherm models [51,56]. The value of the adsorption intensity (n) is very indicative. Therefore, when 1/n < 1 (normal adsorption), 1/n > 1 (cooperative adsorption), while n = 1, depicts zero concentration effect on the partition between the two phases.

Table 2. Adsorption model data for the adsorption of Pb(II), Cd(II) and Ni(II) ions by $Fe_3O_4@SiO_2-NH_2/GO$ under initial concentration 10 mg/L, contact time 30 - 60 min, at room temperature and pH 5 - 7.5.

Metal ions	Langmuir				Freundlich	
	q_m (mgg^{-1})	K_L(mgL^{-1})	R^2	n	K(mgg^{-1})	R^2
Pb(II)	13.46	1.276	0.99956	4.14989	6.84195	0.90481
Cd(II)	18.58	0.797	0.99461	3.13195	7.92885	0.9713
Ni(II)	13.52	0.292	0.98976	2.60688	3.84911	0.85191

3.9.6 Adsorption kinetics

The investigation of adsorption kinetics unveils the adsorption mechanism and the relationship between contact time and adsorption amount of metal ions Pb(II), Cd(II) and Ni(II) (Fig. 14(a) – (b)). In this study, metal ion adsorption studies were investigated for both the pseudo-first-order and pseudo-second-order kinetic models of the kinetic process of the adsorption Pb(II), Cd(II) and Ni(II) by $Fe_3O_4@SiO_2$-NH_2/GO using equations 8 and 9 [57]:

$$Iog(q_e - q_t) = \log q_e - \frac{k_1 t}{2.0303} \tag{8}$$

and

$$t/q_t = 1/q_e^2 k_2 + t/q_e, \tag{9}$$

where k_1 (min^{-1}) and k_2 (mg mg^{-1} min^{-1}) are rate constants, q_e and q_t are the amounts of heavy metal ions, Pb(II), Cd(II) and Ni(II) adsorbed at equilibrium (mg/g) and time t (min), respectively. The exact values of log (q_e − q_t) (Fig. 14(a) and t/q_t (Fig. 14(b)) can be calculated from the experimental results and plotted against contact time, t (min).
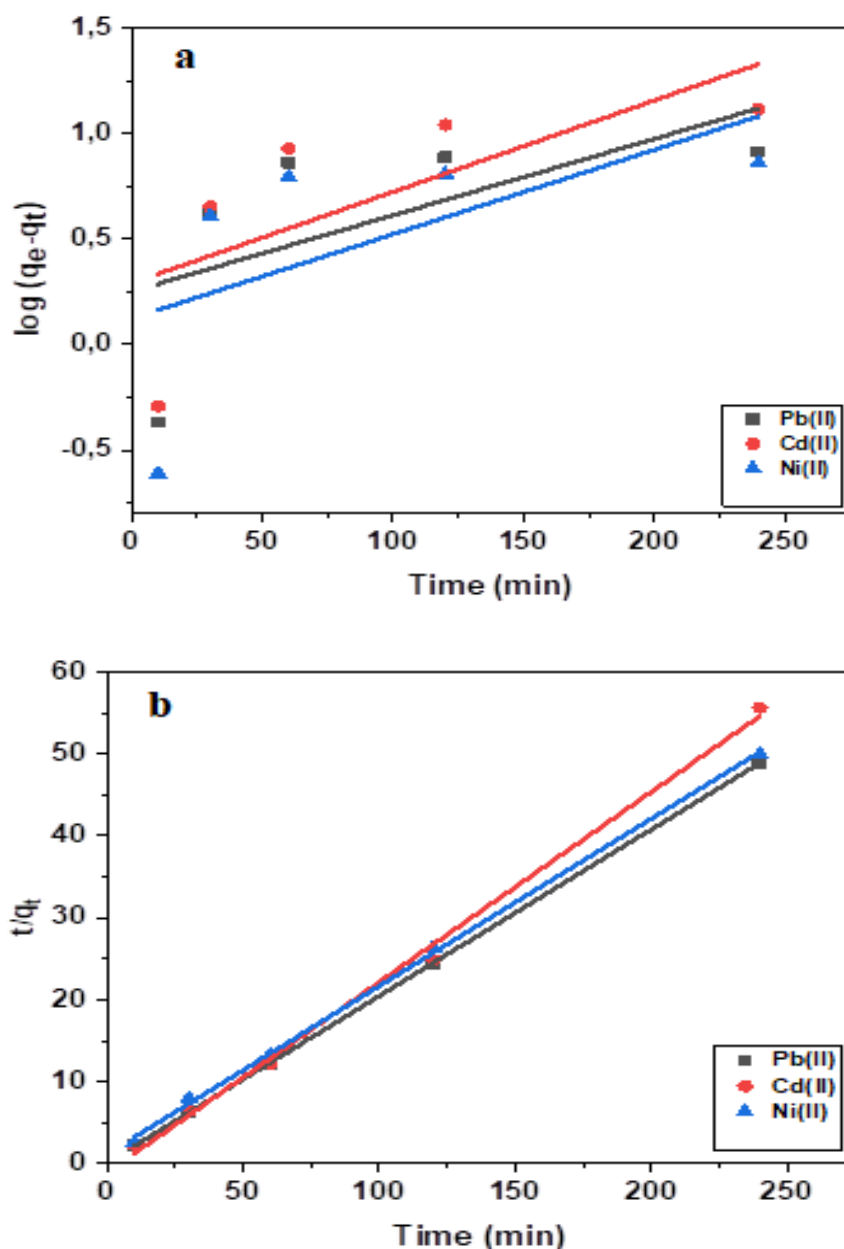
Fig. 14. a) Pseudo-first order and b) Pseudo-second-order kinetics for the adsorption of Pb(II), Cd(II) and Ni(II) ions by $Fe_3O_4@SiO_2-NH_2/GO$.

The data for the kinetic models shown in Table 3 for Pb(II), Cd(II) and Ni(II), showed the linear regression coefficients (R^2) of the pseudo-second-order kinetic model to be, $R^2 = 0.99998$ for Pb(II), $R^2 = 0.9965$ for Cd(II) and $R^2 = 0.99916$ Ni(II), respectively.

Table 3. Kinetic parameters for the adsorption of Pb(II), Cd(II) and Ni(II) ions by $Fe_3O_4@SiO_2-NH_2/GO$ under initial concentration 10 mg/L, contact time 30-60 min, at room temperature and pH 5-7.5.

Kinetic parameters	Heavy metal ions		

	Pb(II)	Cd(II)	Ni(II)
Pseudo first-order			
k_1 (min^{-1})	1.504×10^{-5}	1.8×10^{-5}	1.6625×10^{-5}
$q_{e,\text{cal}}$ (mgg^{-1})	1.78587	1.95583	1.3311
R^2	0.37726	0.4819	0.35068
Pseudo second order			
k_2 (gmg^{-1}min^{-1})	2.7675×10^{-1}	-5.1185×10^{-2}	3.434964×10^{-2}
$q_{e,\text{cal}}$ (mgg^{-1})	4.92368	4.31220	4.89524
R^2	0.99998	0.9965	0.99916

These values were much higher than the R^2 values of the pseudo-first-order kinetic model. The calculated qe values of the pseudo-second- order equation (Table 3) for all the three heavy metals Pb(II) (4.924), Cd(II) (4.312) and Ni(II) (4.895) closely matched the experimental qe values. The results confirmed that pseudo-second-order model can better-fit the removal process of Pb(II), Cd(II) and Ni(II) ions by Fe$_3$O$_4$@SiO$_2$-NH$_2$/GO adsorbent and the rate-controlling mechanism involved chemisorption processes.

4. CONCLUSIONS

The Fe$_3$O$_4$@SiO$_2$-NH$_2$/GO nanocomposite was synthesized through a reflux reaction for the comparative removal of Pb(II), Cd(II) and Ni(II) ions from aqueous solution. Experimental results revealed pH dependence for the removal efficiency of the metal ions aqueous solution, with Ni(II) at pH 6, Pb(II) and Cd(II) at pH 7 – 7.5. Enhanced performance of Fe$_3$O$_4$@SiO$_2$-NH$_2$/GO was shown in the adsorption of metal ions, wherein removal efficiencies were observed to be 97.5%, 92.5% and 81.3% for Pb(II), Cd(II) and Ni(II), respectively. Both Pb(II) and Cd(II) ions were adsorbed far much better to the binding sites on Fe$_3$O$_4$@SiO$_2$-NH$_2$/GO compared to Ni(II). The magnetic adsorbent could be separated from solution through the application of an external magnetic field. The experimental results showed that the adsorption nature favoured Langmuir isotherm for all the three metal ions, wherein the Langmuir isotherm $(R)^2$ values were 0.99956, 0.99461 and 0.98876 for Pb(II), Cd(II) and Ni(II), respectively. Equilibrium adsorption data showed the pseudo-second order as the best fit and that chemisorption mechanism was involved. The prepared Fe$_3$O$_4$@SiO$_2$-NH$_2$/GO showed stability and reproducibility after 7 cycles. The presence of amide bonds between amino groups and carboxylic groups enhanced the stability of the nanocomposite. The

synthesized nanocomposite is a promising adsorbent for application in water/wastewater remediation.

CONFLICT OF INTEREST

All the authors hereby accept responsibility for the content of the manuscript. The authors declare no conflict of interest or competing financial interest.

ACKNOWLEDGMENTS

REFERENCES

1. T. Rasheed, M. Bilal, F. Nabeel, M. Adeel, and H. M. N. Iqbal, Environment International **122**, (2019).

2. M. Kumar, J. S. Chung, and S. H. Hur, Applied Sciences (Switzerland) **9**, (2019).

3. L. Cui, Y. Wang, L. Gao, L. Hu, L. Yan, Q. Wei, and B. Du, Chemical Engineering Journal (2015).

4. T. U. For, T. H. E. Remediation, O. F. Cadmium, N. From, and A. Solution, **3**, (2017).

5. M. I. A. Abdel Maksoud, A. M. Elgarahy, C. Farrell, A. H. Al-Muhtaseb, D. W. Rooney, and A. I. Osman, Coordination Chemistry Reviews **403**, (2020).

6. M. ping Wei, H. Chai, Y. li Cao, and D. zeng Jia, Journal of Colloid and Interface Science **524**, (2018).

7. B. Y. Z. Hiew, L. Y. Lee, X. J. Lee, S. Thangalazhy-Gopakumar, S. Gan, S. S. Lim, G. T. Pan, T. C. K. Yang, W. S. Chiu, and P. S. Khiew, Process Safety and Environmental Protection **116**, 262 (2018).

8. A. Abu-Nada, G. McKay, and A. Abdala, Nanomaterials **10**, (2020).

9. R. Zare-Dorabei, S. M. Ferdowsi, A. Barzin, and A. Tadjarodi, Ultrasonics Sonochemistry **32**, (2016).

10. N. P. Raval, P. U. Shah, and N. K. Shah, Journal of Environmental Management **179**, 1 (2016).

11. M. Mahdavi, M. Bin Ahmad, M. J. Haron, Y. Gharayebi, K. Shameli, and B. Nadi, Journal of Inorganic and Organometallic Polymers and Materials **23**, 599 (2013).

12. D. F. Enache, E. Vasile, C. M. Simonescu, A. Răzvan, A. Nicolescu, A. C. Nechifor, O. Oprea, R. E. Pătescu, C. Onose, and F. Dumitru, Journal of Solid State Chemistry **253**, 318 (2017).

13. C. Hou, T. Jiao, R. Xing, Y. Chen, J. Zhou, and L. Zhang, Journal of the Taiwan Institute of Chemical Engineers **78**, 118 (2017).

14. H. C. Vu, A. D. Dwivedi, T. T. Le, S. Seo, E. Kim, and Y. Chang, Chemical Engineering Journal **307**, 220 (2017).

15. S. K. Sahoo and G. Hota, ACS Applied Nano Materials **2**, 983 (2019).

16. V. Ganesan, C. Louis, and S. P. Damodaran, Journal of Environmental Chemical Engineering **6**, 2176 (2018).

17. D. Zhao, X. Gao, C. Wu, R. Xie, S. Feng, and C. Chen, Applied Surface Science **384**, (2016).

18. S. Bao, W. Yang, Y. Wang, Y. Yu, and Y. Sun, Journal of Hazardous Materials **381**, 120914 (2020).

19. D. Wang, G. Zhang, L. Zhou, M. Wang, D. Cai, and Z. Wu, Langmuir **33**, 7007 (2017).

20. V. Ganesan, C. Louis, and S. P. Damodaran, Journal of Environmental Chemical Engineering **6**, 2176 (2018).

21. M. Akbar and M. Manoochehri, Inorganic Chemistry Communications **103**, 37 (2019).

22. R. Doaga, T. Mccormac, and E. Dempsey, (2020).

23. M. Mahdavi, M. Bin Ahmad, J. Haron, F. Namvar, B. Nadi, M. Zaki, A. Rahman, and J. Amin, 7533 (2013).

24. H. Su, Z. Ye, and N. Hmidi, Colloids and Surfaces A: Physicochemical and Engineering Aspects **522**, 161 (2017).

25. D. C. Marcano, D. V. Kosynkin, J. M. Berlin, A. Sinitskii, Z. Sun, A. Slesarev, L. B. Alemany, W. Lu, and J. M. Tour, ACS Nano **4**, 4806 (2010).

26. M. Khazaei, S. Nasseri, M. R. Ganjali, M. Khoobi, R. Nabizadeh, A. H. Mahvi, S.

Nazmara, and E. Gholibegloo, Journal of Environmental Health Science and Engineering **14**, 1 (2016).

27. L. Cui, Y. Wang, L. Gao, L. Hu, L. Yan, Q. Wei, and B. Du, Chemical Engineering Journal **281**, 1 (2015).

28. Z. Sharafi, B. Bakhshi, J. Javidi, and S. Adrangi, Iranian Journal of Pharmaceutical Research **17**, 386 (2018).

29. V. W. O. Wanjeri, C. J. Sheppard, A. R. E. Prinsloo, J. C. Ngila, and P. G. Ndungu, Journal of Environmental Chemical Engineering **6**, 1333 (2018).

30. S. Dubey, S. Banerjee, S. N. Upadhyay, and Y. C. Sharma, Journal of Molecular Liquids **240**, (2017).

31. N. H. Othman, M. Che Ismail, M. Mustapha, N. Sallih, K. E. Kee, and R. Ahmad Jaal, Progress in Organic Coatings **135**, 82 (2019).

32. S. Aslam, F. Mustafa, and M. A. Ahmad, Ceramics International **44**, 6823 (2018).

33. L. Chen, J. Xu, and J. Hu, Journal of Radioanalytical and Nuclear Chemistry **297**, 97 (2013).

34. N. I. Zaaba, K. L. Foo, U. Hashim, S. J. Tan, W. W. Liu, and C. H. Voon, Procedia Engineering **184**, 469 (2017).

35. F. Ghasemy-Piranloo, S. Dadashian, and F. Bavarsiha, Journal of Inorganic and Organometallic Polymers and Materials (2020).

36. S. Rahdar, A. Rahdar, M. N. Zafar, S. S. Shafqat, and S. Ahmadi, Journal of Materials Research and Technology **8**, 3800 (2019).

37. S. Yang, T. Zeng, Y. Li, J. Liu, Q. Chen, J. Zhou, Y. Ye, and B. Tang, Journal of Nanomaterials **2015**, (2015).

38. J. K. Sahoo, S. K. Paikra, A. Baliarsingh, D. Panda, S. Rath, M. Mishra, and H. Sahoo, Nano Express **1**, 010062 (2020).

39. S. Haq, W. Rehman, and M. Waseem, Journal of Inorganic and Organometallic Polymers and Materials **29**, 651 (2019).

40. M. P. Bilibana, U. Feleni, A. R. Williams, and E. Iwuoha, Processes **9**, 1 (2021).

41. L. Liu, X. Yang, L. Ye, D. Xue, M. Liu, and S. Jia, **174**, 1078 (2017).

42. Z. Lu, J. Yu, H. Zeng, and Q. Liu, Separation and Purification Technology **183**, 249 (2017).

43. N. Ye, Y. Xie, P. Shi, T. Gao, and J. Ma, Materials Science & Engineering C **45**, 8 (2014).

44. Y. Yoon, M. Zheng, Y. T. Ahn, W. K. Park, W. S. Yang, and J. W. Kang, Separation and Purification Technology **178**, 40 (2017).

45. A. Shahat, H. M. A. Hassan, H. M. E. Azzazy, E. A. El-Sharkawy, H. M. Abdou, and M. R. Awual, Chemical Engineering Journal **332**, 377 (2018).

46. K. K. Kefeni, B. B. Mamba, and T. A. M. Msagati, Separation and Purification Technology **188**, 399 (2017).

47. A. Shahbazi, N. N. Marnani, and Z. Salahshoor, Biocatalysis and Agricultural Biotechnology **22**, 101398 (2019).

48. M. Sun, P. Li, X. Jin, X. Ju, W. Yan, J. Yuan, and C. Xing, Food and Agricultural Immunology **29**, 1053 (2018).

49. D. Vilela, J. Parmar, Y. Zeng, Y. Zhao, and S. Sánchez, Nano Letters **16**, (2016).

50. R. L. White, C. M. White, H. Turgut, A. Massoud, and Z. R. Tian, Journal of the Taiwan Institute of Chemical Engineers **85**, (2018).

51. M. Anbia and M. Haqshenas, International Journal of Environmental Science and Technology **12**, (2015).

52. A. I. A. Sherlala, A. A. A. Raman, M. M. Bello, and A. Asghar, Chemosphere **193**, 1004 (2018).

53. C. S. C. Chiew, H. K. Yeoh, P. Pasbakhsh, P. E. Poh, B. T. Tey, and E. S. Chan, Polymer Degradation and Stability **123**, 146 (2016).

54. M. K. Mohammadi Nodeh, S. Soltani, S. Shahabuddin, H. Rashidi Nodeh, and H. Sereshti, Journal of Inorganic and Organometallic Polymers and Materials **28**, 1226 (2018).

55. N. C. Joshi, A. Gaur, and A. Singh, Journal of Inorganic and Organometallic Polymers and Materials (2020).

56. X. Hu, J. Xu, C. Wu, J. Deng, W. Liao, Y. Ling, Y. Yang, Y. Zhao, Y. Zhao, X. Hu, H. Wang, and Y. Liu, PLoS ONE **12**, 1 (2017).

57. Z. Hu, S. Qin, Z. Huang, Y. Zhu, L. Xi, and Z. Li, Journal of Environmental Chemical Engineering **5**, (2017).